Chemical Science

ROYAL SOCIETY OF CHEMISTRY

EDGE ARTICLE

View Article Online
View Journal | View Issue

Cite this: *Chem. Sci.*, 2025, **16**, 4311

All publication charges for this article have been paid for by the Royal Society of Chemistry

Coordination-in-pipe engineering of Pt-based intermetallic compounds with nanometer to angstrom precision†

Shouyao Hu,[a] Jiaxin Gong,[a] Yu Tao,[a] Runze Ma,[a] Jianping Guan,[a] Xu Liu,[a] Jinhua Hu,[a] Jun Yan, *[a] Shibin Wang,[b] Zedong Zhang,[c] Xiao Liang,[c] Zechao Zhuang,[cd] Yunhu Han, [e] Xusheng Zheng, [f] Wensheng Yan, [f] Chengjin Chen,[g] Wei Zhu, [g] Dingsheng Wang [c] and Yu Xiong *[a]

The simultaneous regulation of particle size, surface coordinated environment and composition for Pt-based intermetallic compound (Pt-IMC) nanoparticles to manipulate their reactivity for energy storage is of great importance. Herein, we report a general synthetic method for Pt-IMCs using SBA-15 for coordination-in-pipe engineering. The particle size can be regulated to 3–9 nm by carrying out the coordination in pipes with different diameters and the coordination number of the interface metal atoms can be adjusted by altering the N source. Moreover, this strategy can also be expanded to the synthesis of Pt-IMCs with the majority of fourth period transition metals (Ti, V, Cr, Mn, Fe, Co, Ni, Cu, Zn). The Pt_3Co IMC using 1,10-phenanthroline as the nitrogen source (Pt_3Co@CN) shows the highest catalytic performance in the methanol oxidation reaction (MOR; 2.19 A mg_{Pt}^{-1}) among the investigated nitrogen sources. The high chemical states of surface Pt and Co, affected by the nitrogen coordination number at the angstrom scale, facilitate electron accumulation on active sites, reduce the activation energy of the rate-determining step and enhance the catalytic performance of Pt-IMCs in the MOR.

Received 22nd November 2024
Accepted 24th January 2025

DOI: 10.1039/d4sc07905a

rsc.li/chemical-science

Introduction

Platinum-based catalysts are widely used as electrode catalysts in various applications, such as proton exchange membrane fuel cells (PEMFC)[1–6] and metal–air batteries[7–9] due to their high catalytic performance in electrode reactions.[10–15] However, the expensive price and scarce reserves restrict their potential applications.[16,17] The addition or alloying of another metal is a useful strategy, which not only reduces the Pt dosage but also increases the catalytic performance *via* synergistic effects.[18–24] Nevertheless, segregation always occurs in the disordered nanoalloy, leading to unmeasurable, diversified active sites, and uncertain structure–performance relationships.[25–28] Intermetallic compounds (IMCs) possess long-range ordered structures, in which Pt atoms are regularly arranged at the atomic level, regulating the catalytic performance of Pt through electronic effects and improving their atomic utilization rate, which is more conducive to in-depth study of the relationships between properties and structure.[29–33]

Developing synthetic strategies towards IMCs has attracted much attention in recent years. The solvothermal strategy efficiently adjusts the morphology *via* a capping agent-assisted crystallization process, while an obstacle to downsizing IMCs *via* solvothermal strategy is difficult to overcome, which means dissipating a large amount of inner Pt sites.[34–37] Recently, several studies have been reported using a pyrolysis-based strategy,[38–40] which can efficiently synthesize small sized IMCs (*ca.* 5 nm). For example, Yang *et al.*[41] developed a general sulfur-anchoring strategy to obtain Pt-based IMCs with different elements, which show high catalytic performance in the acidic oxygen reduction reaction. Cheng and co-workers synthesized Pt-IMCs on ZIF-8-derived nitrogen-doped porous carbon by a wet-impregnation method, which exhibited high ORR performance.[42] The unsaturated Pt or M (M = Fe Co Ni *et al.*) atoms on the surface are coordinated by elements with high electronegativity (C, N, O, S *et al.*) on the support of such

[a]*Department of Chemistry and Chemical Engineering, Central South University, Changsha 410083, China. E-mail: yanjun@csu.edu.cn; thomas153@126.com*

[b]*College of Chemical Engineering, Zhejiang University of Technology, Hangzhou 310032, China*

[c]*Department of Chemistry, Tsinghua University, Beijing 100084, China*

[d]*Department of Chemical Engineering, Columbia University, New York, NY, 10027, USA*

[e]*Frontiers Science Center for Flexible Electronics, Xi'an Institute of Flexible Electronics (IFE) and Xi'an Institute of Biomedical Materials & Engineering, Northwestern Polytechnical University, Xi'an 710072, China*

[f]*National Synchrotron Radiation Laboratory, University of Science and Technology of China, Hefei 230029, China*

[g]*State Key Lab of Organic-Inorganic Composites, Beijing Advanced Innovation Center for Soft Matter Science and Engineering, Beijing University of Chemical Technology, Beijing 100029, China*

† Electronic supplementary information (ESI) available. See DOI: https://doi.org/10.1039/d4sc07905a

catalysts,[43–49] and thus the electrons will transfer from the Pt or M to the coordinated element, which effectively adjusts their catalytic performance, especially among small particles with a higher ratio of surface anchoring metal atoms. Additionally, owing to the discontinuous molecular orbitals in small nanoparticles, manipulating the particle size of IMCs is also vital to realizing their catalytic performance.[50–53] The reported works concentrated more on the IMCs loaded on settled coordinated sites of the prefabricated support. For example, the synthesis of Pt-IMCs on an S-containing support results in smaller particle sizes (<5 nm), while using only N- or O-containing groups will remarkably increase the particle size,[54] indicating that it is irresolvable to manipulate the particle size with the same coordinated environment and precisely adjust their catalytic performance by this strategy.

Due to their high surface area, thermostability, and porosity, zeolites are widely used as a hard template to synthesize porous carbon.[41,55] Among those zeolites, SBA-15 possesses ordered pipes with adjustable diameter, which could be an ideal template to control the particle sizes of IMCs.[56,57] The pipe-like mesopores can effectively hinder the growth and regulate the particle size of IMCs. Herein, we report a general synthetic method for Pt-based IMCs (PtM; M = Ti, V, Cr, Mn, Fe, Co, Ni, Cu, Zn) with controllable size and coordinated surface sites on a nitrogen-doped carbon catalyst using SBA-15 for coordination-in-pipe engineering. The particle sizes can be controlled by regulating the pipe diameter of SBA-15 at the nanoscale (3–9 nm). The chemical states of Pt and Co can also be manipulated by adjusting the coordination number with nitrogen at the angstrom scale, which is ascribed to the composition and structure of the N sources before pyrolysis. Moreover, the as-synthesized Pt_3Co using 1,10-phenanthroline as the N source shows the highest catalytic performance in the methanol oxidation reaction (MOR) with a mass activity of 2.19 A mg_{Pt}^{-1}, which is much higher than that of Pt_3Co synthesized using other N sources. Density functional theory (DFT) combined with experimental results illustrate that the high chemical state of the metals effectively facilitates electron accumulation at the active sites, reducing the free energy of the intermediate states, and the activation energy of the rate-determining step (*CO–*COOH) in the MOR, which accelerates the reaction.

Results and discussion

Synthesis and structural characterization of Pt_3Co@CN

The typical schematic illustration of Pt-IMCs is shown in Fig. 1a. Pt and M precursors (M = Ti, V, Cr, Mn, Fe, Co, Ni, Cu, Zn) are first coordinated with an N source (1,10-phenanthroline, *etc.*) and adequately mixed with SBA-15 in a solution containing water and ethanol to ensure full coordination. During the subsequent process, the solvent outside of the pipes evaporates first, concentrating the solution and ensuring the complexes containing Pt (M) and N source finally remain in the pipes of SBA-15. The obtained solid is pyrolyzed at high temperature (~1000 °C) and then etched with NaOH to obtain the Pt-IMCs (Table S1†). The synthetic scale of this strategy can be enlarged to gram scale (Fig. S1†). In this strategy, the growth of Pt-IMCs is inhibited by the limited diameter of the pipes from the radial direction and the nitrogen-doped carbon from the longitudinal direction. Therefore, the size of Pt-IMCs can be

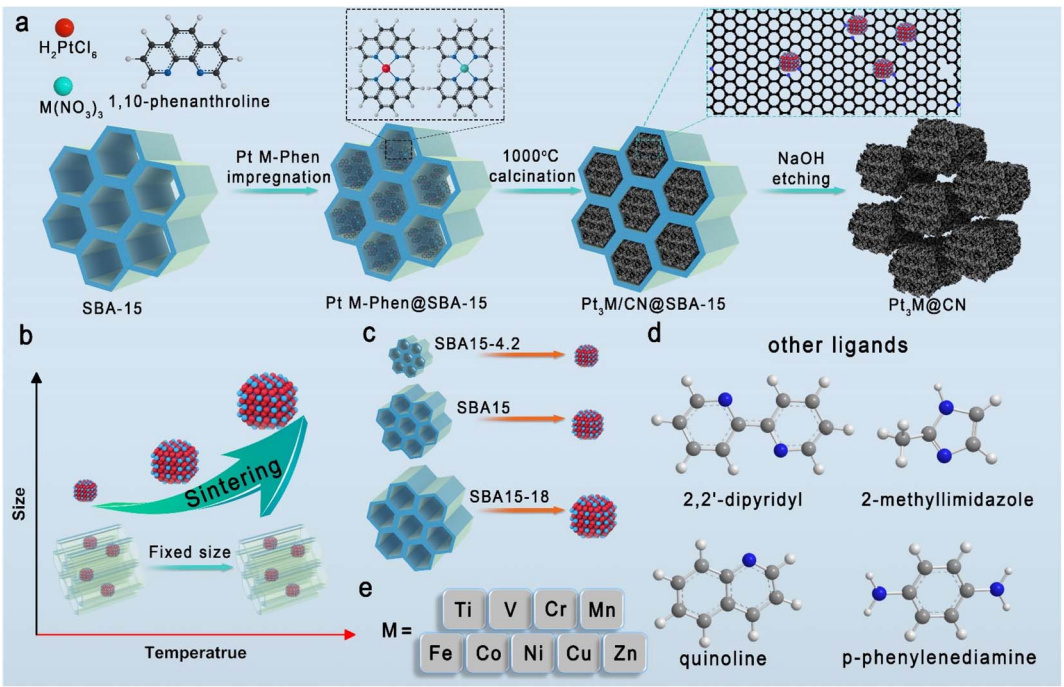

Fig. 1 The schematic diagram. (a) The schematic illustration of synthetic methods involved in this study. (b) The particle sizes vary with temperature in the absence/presence of SBA-15. (c) Manipulating the particle sizes of Pt-IMCs. The scanning of (d) nitrogen sources and (e) subsidiary metals involved in this study.

manipulated by changing the pipe diameter of SBA-15 (Fig. 1b and c). Moreover, the coordination numbers between the metal and the nitrogen can also be regulated by using different N sources (Fig. 1d). Pt-IMCs with different subsidiary metals can also be successfully synthesized by modifying the category of M precursor (Fig. 1e).

Pt_3Co IMCs, synthesized using 1,10-phenanthroline and SBA-15 (average diameter: 8 nm), are taken as an example (namely, Pt_3Co@CN) to illustrate the typical characterization of Pt-IMCs involved in this study. The broad peaks, especially the superlattice diffraction peak (located at 32.8°) in the powder X-ray diffraction (XRD) pattern, can be attributed to Pt_3Co IMCs, which matches with the Joint Committee on Powder Diffraction Standards (JCPDS PDF#29-0499; Fig. 2a). From the transmission electron microscopy (TEM) images, we can observe that Pt_3Co@CN maintained the pipe-like mesoporous features of the original SBA-15 (Fig. S2 and S3†). Numerous nanoparticles with an average size of 4.5 nm can be observed in the TEM images (Fig. 2b). From energy dispersive X-ray spectroscopy (EDS) mapping, Pt and Co are mainly detected in the nanoparticles, and N is homogeneously dispersed in the support (Fig. 2c). Owing to the different Z-contrast, Pt–Pt and Co–Pt–Co atomic columns can be clearly identified in the aberration-corrected high-angle annular dark-field scanning transmission electron microscopy images (AC-HAADF-STEM; Fig. 2d and e), which matches well with the corresponding crystal model (the inset of Fig. 2e). The corresponding fast Fourier transform (FFT) pattern shows that Pt_3Co IMC is oriented along the $[0\bar{1}1]$ direction (the inset of Fig. 2d) with the lattice spacings measured to be 0.384 nm and 0.279 nm, which can be attributed to the (100) and (110) planes of Pt_3Co ($Pm\bar{3}m$), respectively.

To explore the effect of the pipe diameter on the size of the IMCs, SBA-15 samples with average diameters of 4 nm and 18 nm (characterization is shown in Fig. S4–S6†) were used (named Pt_3Co (4) and Pt_3Co (18), respectively). With increasing average pipe diameter, the half peak width in the XRD pattern

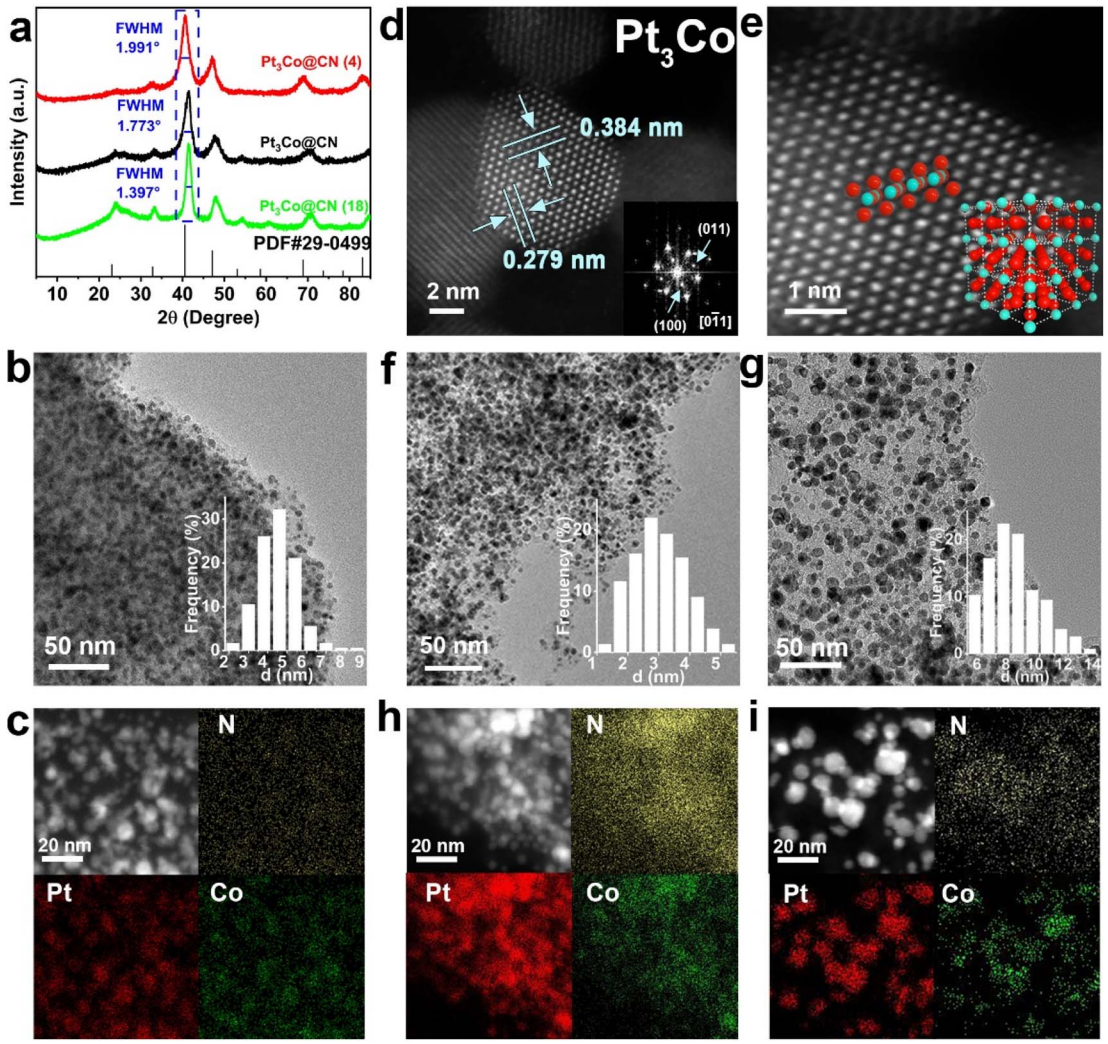

Fig. 2 Characterization of Pt_3Co IMCs. (a) XRD patterns for Pt_3Co IMCs. (b) TEM image of Pt_3Co@CN. The inset is the corresponding size distribution. (c) EDS elemental mapping of Pt_3Co@CN. (d) AC-HAADF-STEM (the inset is the corresponding FFT pattern) and (e) the partial enlarged image of Pt_3Co@CN (the inset is the corresponding crystal model). (f and g) TEM images of Pt_3Co (4) and Pt_3Co (18), respectively. (h and i) EDS elemental mappings of Pt_3Co (4) and Pt_3Co (18), respectively.

becomes sharper, suggesting an increase in the IMCs size (Fig. 2a). The average particle sizes of Pt_3Co (4) and Pt_3Co (18) were 3.02 nm, and 8.24 nm, respectively (Fig. 2f and g) with Pt and Co concentrated in the nanoparticles and N distributed in the support (Fig. 2h and i). Moreover, the synthesis of Pt_3Co without SBA-15 leads to phase separation (disordered PtCo alloy and Pt) and larger particle size (*ca.* 38 nm; Fig. S7†). When synthesizing without a N source, IMC nanoparticles will grow out of the pipes, resulting in larger nanoparticles (*ca.* 16 nm; Fig. S8†). These results illustrate that (1) SBA-15 inhibits both the growth of IMCs and the phase separation of Pt and Co; (2) the carbonization of 1,10-phenanthroline hinders the migration of Pt and Co along the pipes. Furthermore, this strategy can also work with other mesoporous zeolites. When hollow silica with spherical mesopores is used in the synthesis, Pt_3Co IMCs with an average particle size of 7.8 nm (Pt_3Co@mshs; Fig. S9†) are also successfully obtained.

Structural characterization of Pt_3Co (N sources) and Pt_3M@CN

Nitrogen, possessing high electronegativity, coordinates with surface Pt atoms and accepts the electrons from metal atoms in IMCs, which can influence the catalytic performance of Pt by regulating its charge distribution. Different contents and types of nitrogen in IMCs may have different effects on the catalytic performance *via* the strong metal-support interactions. 2,2′-Dipyridyl (dipy), quinoline (quin), *p*-phenylenediamine (pphen) and 2-methylimidazole (mim) possess different aromatic structures or nitrogen types to 1,10-phenanthroline, which may also affect the nitrogen type or content in Pt_3Co@CN [namely, Pt_3Co (N sources)]. XRD patterns combined with EDS mappings demonstrated the ordered intermetallic phases in Pt_3Co (N sources) (Fig. S10–S17†). The Brunauer–Emmett–Teller isotherms do not show striking differences among Pt_3Co (N sources) with the surface area calculated to range from 87.8 to 247.7 $m^2\ g^{-1}$ (Fig. S18 and Table S2†). Though average particle sizes are counted in a narrow range from 3.88 to 4.68 nm, the order of nanoparticle sizes in the Pt-IMCs (Pt_3Co (min), Pt_3Co (pphen), Pt_3Co (quin), Pt_3Co@CN and Pt_3Co (dipy)) follows the order of the molecular sizes of the N sources (Fig. S19–S22 and Table S3†). This result indicates that smaller N sources may fill more space in the pipes of SBA-15, which hinders the further growth of IMCs thus the smaller sizes of IMCs. Surprisingly, the content of Pt (8.84–39.72 wt%) and Co (0.69–4.91 wt%), certified by inductively coupled plasma optical emission spectroscopy (ICP-OES), shows huge variances among Pt_3Co (N sources) (Table S4†). This may be attributed to the stability differences between the Pt complexes with different nitrogen sources during high-temperature annealing.

To further explore the influence of the nitrogen source on the microstructure of Pt_3Co IMCs, a series of characterizations for Pt_3Co@CN, Pt_3Co (quin) and Pt_3Co (mim) are carried out. X-ray photoelectron spectroscopy (XPS) survey spectra show that C, N, Co, and Pt are the primary elements in Pt_3Co (N sources) (Fig. S23†). Three deconvoluted peaks, attributed to graphitic C (284.8 eV), C=C–N (286.2 eV) and C–C=N (288.4 eV), were observed in the C 1s spectra,[58,59] which are almost identical with an average deviation of less than 1.0% (Table S5 and Fig. S24–S26†). The deconvoluted N 1s peaks at 398.6, 399.5, 400.5, and 401.8 eV can be ascribed to pyridinic, coordinated (Pt/Co–N), pyrrolic, and graphitic N, respectively[60,61] (Fig. 3a). Surprisingly, though the microenvironment and the coordinated structure

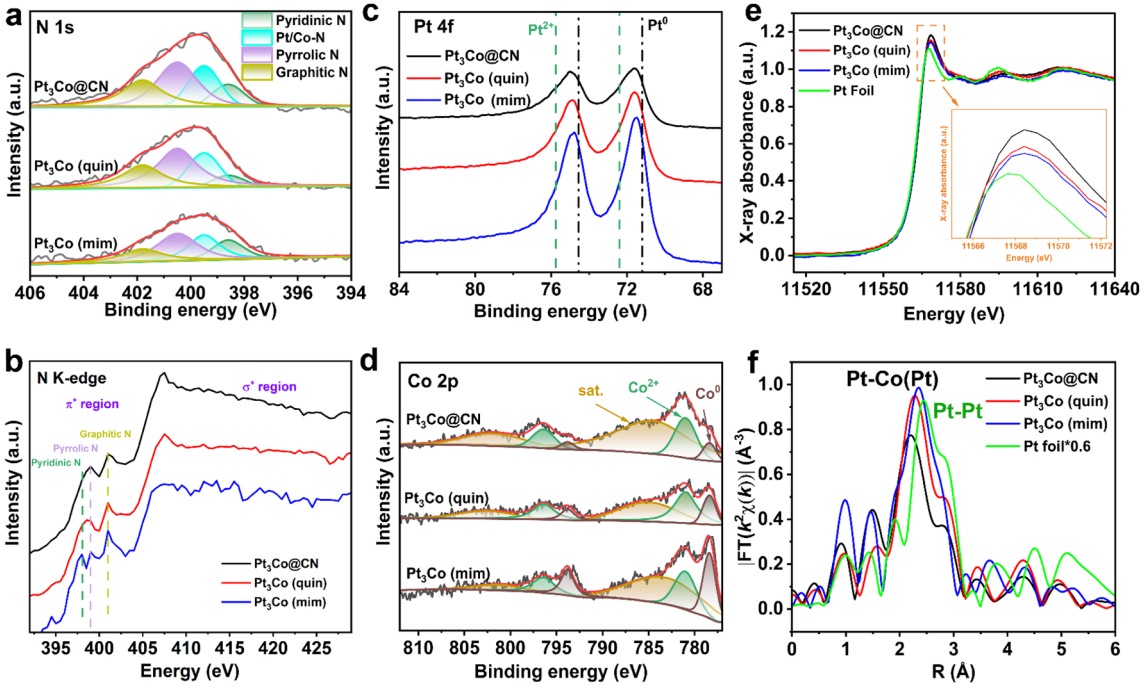

Fig. 3 Characterization of Pt_3Co (N sources). (a) N 1s XPS, (b) N K-edge NEXAFS, (c) Pt 4f XPS and (d) Co 2p XPS spectra of Pt_3Co@CN, Pt_3Co (quin), Pt_3Co (mim). (e) Pt L_3-edge XANES and (f) FT-EXAFS spectra of Pt_3Co@CN, Pt_3Co (quin), and Pt_3Co (mim) with Pt foil as reference.

are different before pyrolysis, only negligible disparity with an average deviation of less than 3.7% in the ratio of N types of Pt_3Co (N sources) can be seen in the N 1s XPS spectra (Table S5†). C K-edge near-edge X-ray absorption fine structure (NEXAFS) spectra (Fig. S27†) exhibit that the spilt resonances[62] at 284.3, 286.4, and 288.9 eV can be attributed to the dipole transitions from the C 1s to π* orbitals of C=C, C–N and C=N, respectively. N K-edge NEXAFS spectra are shown in Fig. 3b; we can find spilt resonances[63] located at 398.1 eV (pyridinic N), 399.0 eV (pyrrolic N), and 401.1 eV (graphitic N), respectively. Notably, the resonances of pyridinic N and pyrrolic N in $Pt_3Co@CN$ are broader than those in the other samples, indicating that more electrons transfer from Pt to N.[64]

The nitrogen contents of $Pt_3Co@CN$, Pt_3Co (quin) and Pt_3Co (mim) were detected using a nitrogen analyser (1.69 wt%, 1.08 wt%, 0.83 wt%, respectively; Table S6†), and are lower than their theoretical nitrogen content (10.75 wt%, 7.67 wt%, 22.68 wt%, respectively). This result may be affected by the degree of decomposition of the N species (15.7%, 14.1%, and 3.6% retained, respectively). Pt and Co chelated coordinated with 1,10-phenanthroline show the highest thermostability, the single-dentate coordination with quinoline shows moderate thermal stability and the large content of excessive nitrogen without coordination in 2-methylimidazole is easier to decompose. Though near 0 chemical state of Pt are detected in the Pt 4f XPS spectra of Pt_3Co (N sources), positive shifts of binding energies in the spectra from Pt_3Co (mim) (0.32 eV), Pt_3Co (quin) (0.40 eV), and $Pt_3Co@CN$ (0.44 eV) to Pt^0 are also detected (Fig. 3c). The deconvoluted signals of Co^{2+} and Co^0 species are detected in the Co 2p XPS spectra[65] and the ratio of Co^{2+} in $Pt_3Co@CN$ is higher than that in Pt_3Co (mim) and Pt_3Co (quin) (Fig. 3d). Moreover, the increasing trend of the chemical state of Co and Pt is correlated with that of nitrogen content in Pt_3Co (N sources). According to the results from the N 1s XPS and K-edge NEXAFS spectra combined with ICP-OES, the ratios of coordinated N are similar among the Pt_3Co (N sources), but the highest nitrogen content leads to the transference of most electrons from the IMCs to nitrogen and thus the highest chemical state of Co and Pt in $Pt_3Co@CN$. Additionally, to explore the effect of the metal content on the chemical states, we also synthesize Pt_3Co with different metal dosages (the molar ratio of Pt and Co is not changed; namely, Pt_3Co-*x*, where *x* represents the metal dosage; characterizations are shown in Fig. S28–S31†). The Pt 4f and Co 2p XPS peaks of Pt_3Co-x do not show obvious shifts, proving that the metal content has little effect on the metal valence state (Fig. S32†). However, the impact of varying N sources on the particle size is relatively minor with a standard deviation of 7.6%, compared to the significant influence of different SBA-15 with a standard deviation of 38%.

To further explore the coordination parameters of Pt in Pt_3Co (N sources), Pt L_3-edge X-ray absorption fine structure (XAFS) analysis is performed. According to the X-ray absorption near-edge structure (XANES) spectra of Pt_3Co (N sources) (Fig. 3e), the height of the white line peaks shows the same trends as the Pt 4f XPS spectra [$Pt_3Co@CN$ > Pt_3Co(quin) > Pt_3Co (min)] and slightly higher than that of Pt foil, further confirming that the electrons of surface Pt are transferred to N in the IMCs. The main peaks in the Fourier-transformed EXAFS of Pt_3Co (mim), Pt_3Co (quin) and $Pt_3Co@CN$ are located at 2.35 Å, 2.28 Å, and 2.19 Å, respectively, attributed to the co-existence of Pt–Co and Pt–Pt bonds, which are obviously lower than the Pt–Pt peak (2.45 Å) in Pt foil (Fig. 3f). The notable difference in Pt–Co may be ascribed to different strengths of metal-support interactions in the three samples. Though the signal intensities below 2.0 Å for Pt_3Co (N sources) are all higher than that of Pt foil, which may be ascribed to the Pt–N bond, the relatively low ratio of Pt–N bond can hardly be totally separated from the metallic bond with high coordination number.

To evaluate the generality of this strategy, Pt–M IMCs (M = Ti, V, Cr, Mn, Fe, Ni, Cu and Zn) were prepared. XRD patterns showed that the diffraction peaks of Pt-IMCs matched the corresponding JCPDS standard cards well (Fig. S33–S40†), indicating the successful synthesis of a series of Pt–M IMCs. Small nanoparticles with average sizes ranging from 3.12 to 4.97 nm (Fig. 4a–h, S41–S48 and Table S7†) are distributed on the CN support densely without agglomeration in the TEM images, indicating that the growth of Pt–M IMCs can be inhibited from sintering using this strategy. HAADF-STEM images and corresponding EDS mappings (Fig. S49–S56†) illustrate that Pt and M were both uniformly distributed on nanoparticles. The atomic phase structure of IMCs corresponding to the atomic model crystal can be directly observed by AC-HAADF-STEM (Fig. 4i–p), confirming the high generality of this strategy. The measured atomic column spacing is shown in Table S8,† which is consistent with the theoretical values of the (110) and (100) crystal face spacing. Additionally, S sources, instead of N sources, were also applied in the synthesis of IMCs. Though the S sources can also hinder the growth of IMCs, the intensity of the superlattice diffraction peak becomes weak, indicating that S sources may not be suitable for this strategy (Fig. S57–S59†).

Methanol oxidation properties of $Pt_3Co@CN$ (N sources)

To evaluate the catalytic performance as well as the structure–performance relationship, MOR was carried out with $Pt_3Co@CN$, Pt_3Co (quin), and Pt_3Co (mim) as catalysts. Benefitting from the small sizes and high metal loading, Pt_3Co (N sources) exhibit high electrochemically active surface areas (ECSA) of 68.0–81.3 $m^2\ g^{-1}$ (Fig. 5a and Table S9†), nearing that of commercial Pt/C (81.0 $m^2\ g^{-1}$). $Pt_3Co@CN$ shows the highest mass-specific activity of 2.19 A mg_{Pt}^{-1} in acidic solution, which is 5.3 times higher than that of commercial Pt/C (0.41 A mg_{Pt}^{-1}; Fig. 5b) and one of the best reported MOR catalysts as far as we know (Fig. 5c and Table S10†). The results of the accelerated durability (ADT) test exhibit that $Pt_3Co@CN$ also retains 75.6% and 60.4% of its mass current density after 1200 and 3600 cycles, respectively, while commercial Pt/C loses 44.4% of its activity after only 1200 cycles (Fig. 5d, S60 and S61†). From the STEM and corresponding EDS mapping of $Pt_3Co@CN$ after the ADT test, no obvious change is detected (Fig. S62†), illustrating the high stability of $Pt_3Co@CN$.

Pt_3Co (quin) shows a good mass activity of 1.26 A mg_{Pt}^{-1} and Pt_3Co (mim) exhibits a moderate mass activity of 0.48 A mg_{Pt}^{-1}. Additionally, $Pt_3Co@CN$ shows the lowest onset potential (0.45

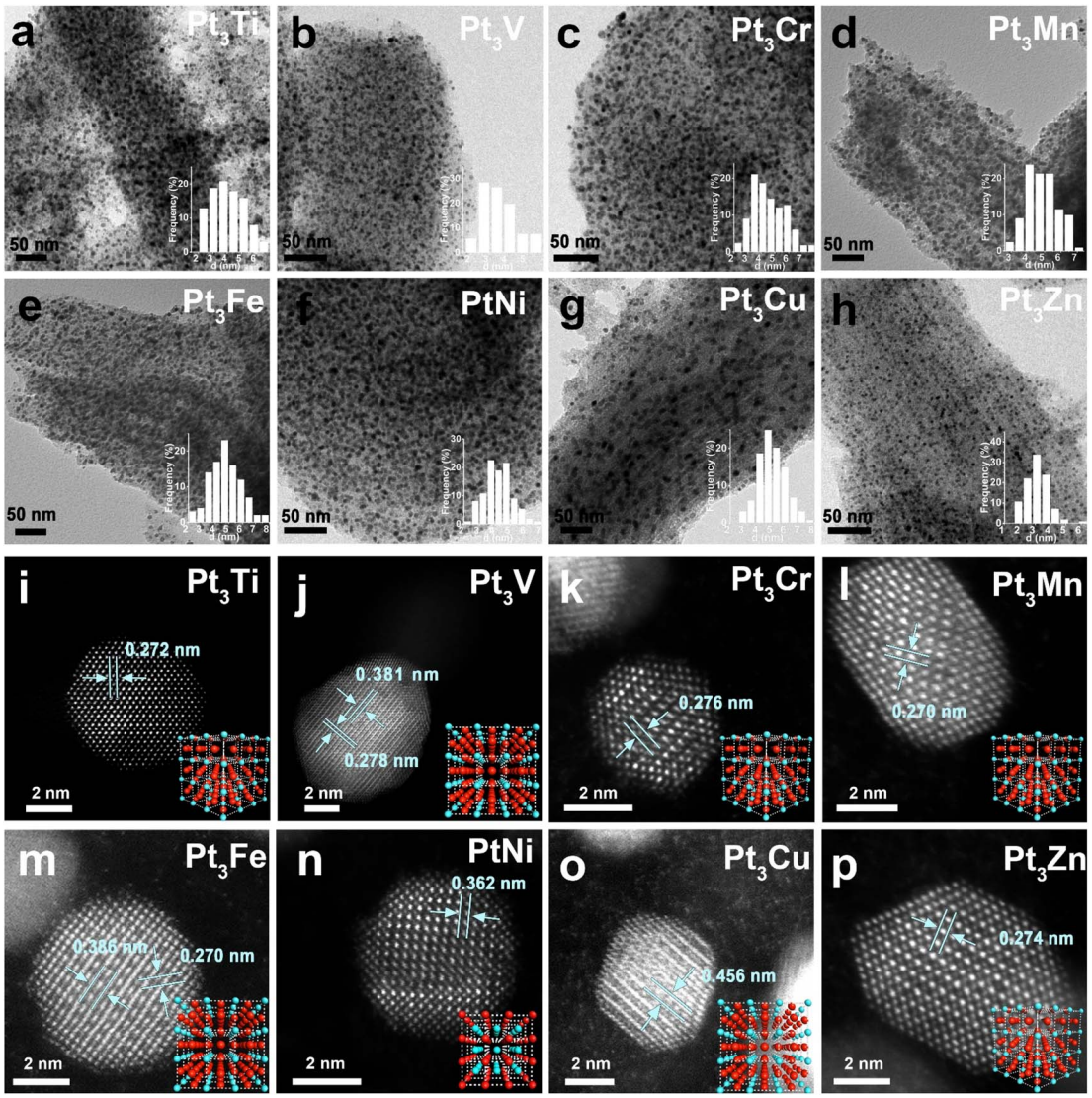

Fig. 4 Characterization of Pt-M IMCs. (a–h) TEM images and (i–p) AC-HAADF-STEM images of Pt_3Ti, Pt_3V, Pt_3Cr, Pt_3Mn, Pt_3Fe, PtNi, Pt_3Cu and Pt_3Zn, respectively. Insets in (a–h) show the corresponding statistical particle size distributions. Insets in (i–p) show the atomic model corresponding to the crystal face.

V) and Pt_3Co (min) (0.63 V) is even more positively shifted than commercial Pt/C (0.58 V). These results suggest that the chemical states of Pt and Co, which are attributed to the different nitrogen contents in the catalysts, can highly affect the MOR performance (Fig. 5e). Moreover, the ratio of forward current and reverse current (I_f/I_b) of Pt_3Co IMCs shows no obvious difference and is much higher than that of commercial Pt/C (Fig. 5f), indicating that the CO resistance is improved by the formation of IMCs.

To further investigate the catalytic mechanism of MOR catalyzed by Pt_3Co@CN, *in situ* Fourier transform infrared (FTIR) analysis is performed (Fig. S63†). The peak with high absorbance, located at 1659 cm^{-1} in the potential range from 0.7–1.2 V, can be attributed to the HCOO*, indicating that HCOO* is the key intermediate in this reaction.[66] Two positive peaks located at 2054 cm^{-1} and 2341 cm^{-1} can be ascribed to the linear absorption of CO and the formation of CO_2 in the potential range from 0.6–1.2 V,[67] suggesting that the poisoning of CO and the desorption of CO_2 do not affect the reactivity of Pt_3Co@CN.

To further explore the influence of the nitrogen content and coordination environment on the MOR performance, DFT calculations were subsequently carried out. Upon formation of the Pt–N bond in Pt_3Co@CN, the heterointerfaces between the (110) facet of Pt_3Co IMCs and support are fabricated. The surface Pt and Co atoms in Pt_3Co are coordinated by the nitrogen of the support with different coordination numbers (Pt_3Co–N_8 and Pt_3Co–N_{12}; Fig. S64†). As shown in Fig. 5g, S65 and S66,† Pt_3Co–N_{12} shows a lower global free energy profile in the reaction process than Pt_3Co–N_8. Moreover, the reaction energy for the elementary step of CO* hydrogenation to COOH* was calculated to be 0.69 eV on the Pt_3Co–N_{12} surface, which is

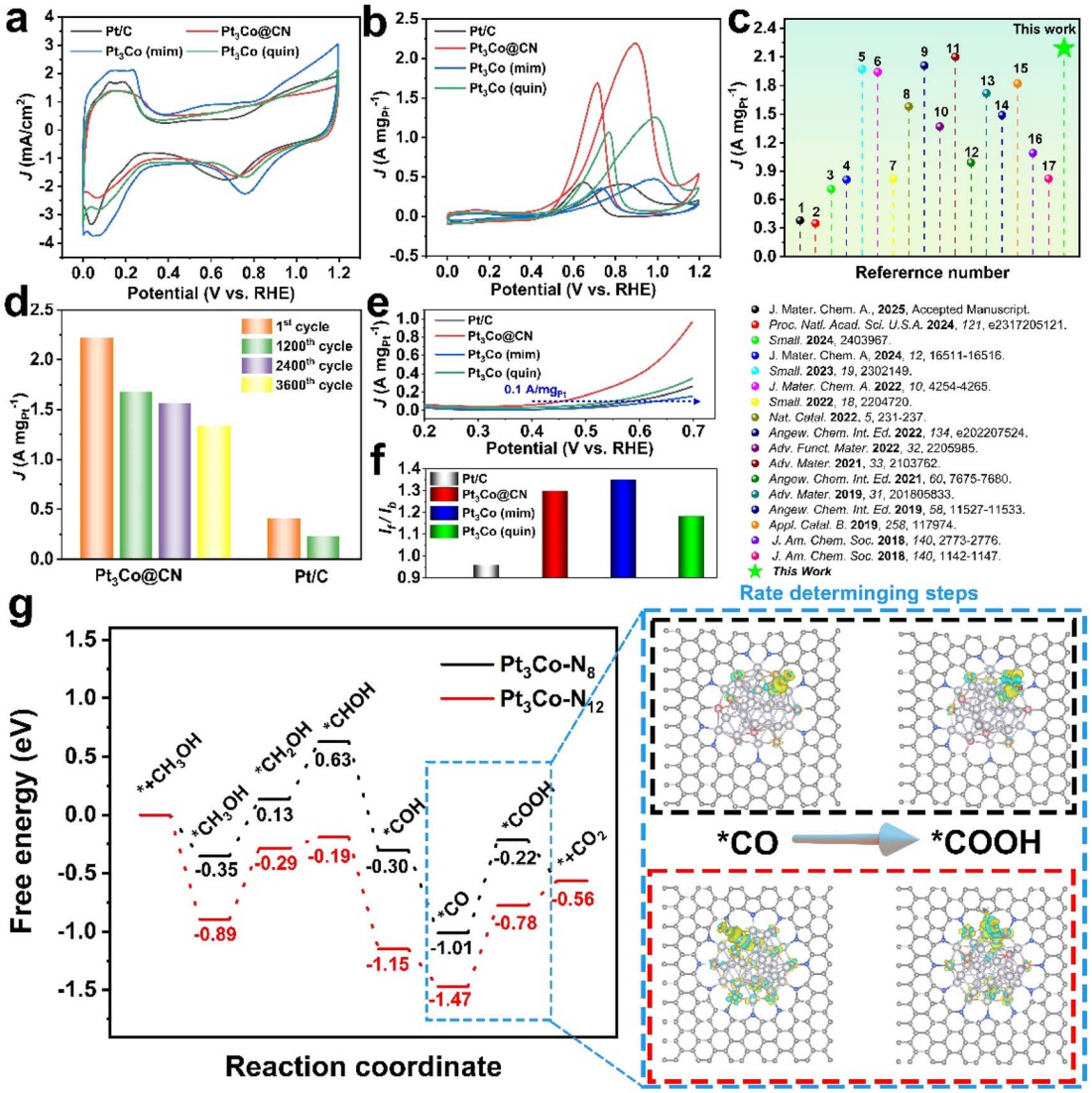

Fig. 5 Methanol electro oxidation. CV curves of Pt_3Co (N sources) with 20% Pt/C as reference in (a) 0.5 M H_2SO_4 and (b) 0.5 M H_2SO_4 + 0.5 M CH_3OH. (c) Comparison of the mass activity of Pt_3Co@CN with recently reported catalysts. (d) The mass activity of Pt_3Co@CN and Pt/C before and after ADT tests. (e) Linear sweep voltammogram curves. (f) The ratio of forward peak current (I_f) to reverse peak current (I_b). (g) Calculated free energy diagram of elementary steps involved in the MOR on the $Pt_3Co–N_8$ and the $Pt_3Co–N_{12}$ surfaces. The charge density difference plots (blue rectangle) for the potential-determining step on $Pt_3Co–N_8$ (black dotted line) and $Pt_3Co–N_{12}$ (red dotted line), respectively. The grey, blue, white, orange and red balls represent C, N, Pt, Co and O, respectively. Blue and yellow contours represent charge loss and charge accumulation, respectively.

0.10 eV lower than that on the $Pt_3Co–N_{12}$ surface, indicating the higher reactivity of the $Pt_3Co–N_{12}$ surface. Bader charge analysis in combination with the charge density difference revealed the electron transference of such key elementary step on both two surfaces. For the CO* intermediate on the $Pt_3Co–N_8$ surface, the electrons transfer from the Pt_3Co cluster to the CO* fragment with the Bader charge value (Δq) calculated to be 0.20 |e|. With the CO* electrocatalytic oxidation to COOH*, electrons transferred from the Pt_3Co cluster to the COOH* fragment with valence electron accumulation of 0.35 |e|, whereas on the $Pt_3Co–N_{12}$ surface, electron transferences from the substrate to the two adsorbates were calculated to be 0.11 |e| and 0.19 |e| for the two adsorbates, respectively, which is less than those on the $Pt_3Co–N_8$ surface. These results indicate that the higher N coordination number leads to a higher electron share from the Pt_3Co cluster, therefore facilitating electron accumulation on the active sites and enhancing the MOR reactivity.

Conclusions

We reported a general coordination-in-pipe engineering strategy for nano-sized Pt-M IMCs. In this strategy, the nanoparticle size can be adjusted by changing the pipe diameter in SBA-15; the number of surface metal atoms can be regulated by changing the N source. Pt-based IMCs with other fourth period transition metals (Ti, V, Cr, Mn, Fe, Co, Ni, Cu and Zn) can also

be synthesized using this strategy. Moreover, Pt_3Co@CN showed the highest electrocatalytic MOR mass activity (2.19 A mg_{Pt}^{-1}) of the Pt_3Co synthesized by different N sources. DFT calculations show that the high chemical states of Pt and Co share more electrons from the Pt_3Co and boost the electron accumulation, which enhances the MOR performance.

Data availability

The authors confirm that the data supporting the findings of this study are available within the article or its ESI.†

Author contributions

Shouyao Hu performed the experiments, analysed the experimental data and wrote the paper. Jiaxin Gong, Yu Tao, Runze Ma, Jianping Guan, Xu Liu, Jinhua Hu and Yunhu Han helped with the data analysis. Jun Yan helped with data analysis and discussions. Shibin Wang helped with DFT calculations, Zedong Zhang, Xiao Liang, and Zechao Zhuang helped with the analysis of XAFS data. Chengjin Chen and Wei Zhu helped with the *in situ* FT-IR spectra. Xusheng Zheng, and Wensheng Yan helped with the analysis of the NEXAFS spectra. Dingsheng Wang and Yu Xiong helped with data analyses, discussions and wrote the paper.

Conflicts of interest

There are no conflicts to declare.

Acknowledgements

This work was financially supported by the National Natural Science Foundation of China (No. 22325101, 22102218), the Science and Technology Innovation Program of Hunan Province (No. 2022RC1110) and the Young Elite Scientists Sponsorship Program by CAST (No. 2022QNRC001). We thank the BL10B station at the National Synchrotron Radiation Laboratory (NSRL) for NEXAFS measurements. We thank the Anhui Absorption Spectroscopy Analysis Instrument Co., Ltd, and BL11B station in Shanghai Synchrotron Radiation Facility (SSRF) for XAFS measurements and analysis.

Notes and references

1 L. Bu, J. Liang, F. Ning, J. Huang, B. Huang, M. Sun, C. Zhang, Y. Ma, X. Zhou, Q. Li and X. Huang, *Adv. Mater.*, 2023, **35**, 2208672.
2 L. Fan, H. Deng, Y. Zhang, Q. Du, D. Leung, Y. Wang and J. Kui, *Energy Environ. Sci.*, 2023, **16**, 1466–1479.
3 E. Zhu, M. Wu, H. Xu, B. Peng, Z. Liu, Y. Huang and Y. Li, *Adv. Funct. Mater.*, 2022, **32**, 2203883.
4 J. Wang, B. Zhang, W. Guo, L. Wang, J. Chen, H. Pan and W. Sun, *Adv. Mater.*, 2023, **35**, 2211099.
5 Z. Qu, Z. An, Z. Ma, N. Li, Y. Han, G. Yang, Q. Jiang, Q. Chen, W. Chu, S. Wang, T. Yu and W. Yang, *ACS Catal.*, 2023, **13**(3), 1856–1862.
6 N. Li, Z. Ou, Y. Liu, X. Yu, T. Wang, Y. Han, Y. Cao and T. Yu, *ACS Appl. Nano Mater.*, 2024, **7**(4), 4423–4429.
7 X. Wang, J. Sunarso, Q. Lu, Z. Zhou, J. Dai, D. Guan, W. Zhou and Z. Shao, *Adv. Energy Mater.*, 2020, **10**, 1903271.
8 R. Gao, J. Wang, Z. Huang, R. Zhang, W. Wang, L. Pan, J. Zhang, W. Zhu, X. Zhang, C. Shi, J. Lim and J. J. Zou, *Nat. Energy*, 2021, **6**, 614–623.
9 M. Xie, X. Xiao, D. Wu, C. Zhen, C. Wu, W. Wang, H. Nian, F. Li, M. Gu and Q. Xu, *Nano Res.*, 2024, **17**, 5288–5297.
10 R. Gui, H. Cheng, M. Wang, X. Tai, H. Zhang, C. Liu, X. Cao, C. Chen, M. Ge, H. Wang, X. Zheng, W. Chu, Y. Lin, Y. Xie and C. Wu, *Adv. Mater.*, 2023, **36**, 2307661.
11 X. Hu, Z. Xiao, W. Wang, L. Bu, Z. An, S. Liu, C.-W. Pao, C. Zhan, Z. Hu, Z. Yang, Y. Wang and X. Huang, *J. Am. Chem. Soc.*, 2023, **145**, 15109–15117.
12 C. Dong, X. Wang, Z. Zhu, C. Zhan, X. Lin, L. Bu, J. Ye, Y. Wang, W. Liu and X. Huang, *J. Am. Chem. Soc.*, 2023, **145**, 15393–15404.
13 X. Fan, W. Chen, L. Xie, X. Liu, Y. Ding, L. Zhang, M. Tang, Y. Liao, Q. Yang, X. Z. Fu, S. Luo and J. L. Luo, *Adv. Mater.*, 2024, **36**, 2313179.
14 Y. Da, R. Jiang, Z. Tian, G. Chen, Y. Xiao, J. Zhang, S. Xi, Y. Deng, W. Chen, X. Han and W. Hu, *Adv. Energy Mater.*, 2023, **13**, 2300127.
15 E. Drzymała, G. Gruzeł, J. Depciuch, M. Pawlyta, M. Donten and M. Parlinska-Wojtan, *Nano Res.*, 2020, **13**, 832–842.
16 C. Zhu, J. Yang, J. Zhang, X. Wang, Y. Gao, D. Wang and H. Pan, *Interdiscip. Mater.*, 2024, **3**, 74–86.
17 Y. Shi, Y. Feng, Z. Wang, X. Wang, Y. Jiang, J. Deng, H. Dai and Y. Liu, *Proc. Natl. Acad. Sci. U.S.A*, 2023, **33**, 526–533.
18 W. Yan, X. Wang, M. Liu, K. Ma, L. Wang, Q. Liu, C. Wang, X. Jiang, H. Li, Y. Tang and G. Fu, *Adv. Funct. Mater.*, 2023, **34**, 2310487.
19 Z. Qiao, C. Wang, C. Li, Y. Zeng, S. Hwang, B. Li, S. Karakalos, J. Park, A. Kropf, E. Wegener, Q. Gong, H. Xu, G. Wang, D. Myers, J. Xie, J. Spendelow and G. Wu, *Energy Environ. Sci.*, 2021, **14**, 4948–4960.
20 Z. Zhang, J. Tian, Y. Lu, X. Gou, J. Li, W. Hu, W. Lin, R. Kim and J. Fu, *Angew. Chem., Int. Ed.*, 2022, **61**, e202202017.
21 J. Zhuang and D. Wang, *Mater. Today Catal.*, 2023, **2**, 100009.
22 Y. Han, Y. Xiong, C. Liu, H. Zhang, M. Zhao, W. Chen, W. Chen and W. Huang, *J. Catal.*, 2021, **396**, 351–359.
23 S. Yuan, X. Zhu, H. Li, Z. Hu, Q. Ren, W. Zhao, X. Tang and S. Hu, *Proc. Natl. Acad. Sci. U.S.A*, 2023, **33**, 225–231.
24 G. Chen, W. Chen, R. Lu, C. Ma, Z. Zhang, Z. Huang, J. Weng, Z. Wang, Y. Han and W. Huang, *J. Am. Chem. Soc.*, 2023, **145**, 22069–22078.
25 T. Shen, D. Xiao, Z. Deng, S. Wang, L. An, M. Song, Q. Zhang, T. Zhao, M. Gong and D. Wang, *Angew. Chem., Int. Ed.*, 2024, **63**, e202403260.
26 X. Mu, S. Liu, M. Zhang, Z. Zhuang, D. Chen, Y. Liao, H. Zhao, S. Mu, D. Wang and Z. Dai, *Angew. Chem., Int. Ed.*, 2024, **63**, e202319618.
27 F. Feng, C. Ma, S. Han, X. Ma, C. He, H. Zhang, W. Cao, X. Meng, J. Xia, L. Zhu, Y. Tian, Q. Wang, Q. Yun and Q. Lu, *Angew. Chem., Int. Ed.*, 2024, **63**, e202405173.

28 Y. Li, S. Niu, P. Liu, R. Pan, H. Zhang, N. Ahmad, Y. Shi, X. Liang, M. Cheng, S. Chen, J. Du, M. Hu, D. Wang, W. Chen and Y. Li, *Angew. Chem., Int. Ed.*, 2024, **63**, e202316755.
29 J. Guan, S. Yang, T. Liu, Y. Yu, J. Niu, Z. Zhang and F. Wang, *Angew. Chem., Int. Ed.*, 2021, **60**, 21899–21904.
30 Z. Wang, X. Yao, Y. Kang, L. Miao, D. Xia and L. Gan, *Adv. Funct. Mater.*, 2019, **29**, 1902987.
31 H. Lv, H. Qin, K. Ariga, Y. Yamauchi and B. Liu, *Angew. Chem., Int. Ed.*, 2022, **61**, e202116179.
32 K. Liu, R. Qin and N. Zheng, *J. Am. Chem. Soc.*, 2021, **143**, 4483–4499.
33 M. Xie, Z. Lyu, R. Chen, M. Shen, Z. Cao and Y. Xia, *J. Am. Chem. Soc.*, 2021, **143**, 8509–8518.
34 S. Luo, W. Chen, Y. Cheng, X. Song, Q. Wu, L. Li, X. Wu, T. Wu, M. Li, Q. Yang, K. Deng and Z. Quan, *Adv. Mater.*, 2019, **31**, 1903683.
35 W. Chen, S. Luo, M. Sun, X. Wu, Y. Zhou, Y. Liao, M. Tang, X. Fan, B. Huang and Z. Quan, *Adv. Mater.*, 2022, **34**, 2206276.
36 Q. Nguyen, C. Wang, Y. Shang, A. Janssen and Y. Xia, *Chem. Rev.*, 2023, **123**, 3693–3760.
37 G. Liu, W. Zhou, Y. Ji, B. Chen, G. Fu, Q. Yun, S. Chen, Y. Lin, P. Yin, X. Cui, J. Liu, F. Meng, Q. Zhang, L. Song, L. Gu and H. Zhang, *J. Am. Chem. Soc.*, 2021, **143**, 11262–11270.
38 P. Yin, X. F. Niu, S. B. Li, K. Chen, X. Zhang, M. Zuo, L. Zhang and H. W. Liang, *Nat. Commun.*, 2024, **15**, 415.
39 Y. Wang, N. Gong, H. Liu, W. Ma, K. Hippalgaonkar, Z. Liu and Y. Huang, *Adv. Mater.*, 2023, **35**, 2302067.
40 Q. Cheng, S. Yang, C. Fu, L. Zou, Z. Zou, Z. Jiang, J. Zhang and H. Yang, *Energy Environ. Sci.*, 2022, **15**, 278–286.
41 C. Yang, L. Wang, P. Yin, J. Liu, M. Chen, Q. Yan, Z. Wang, S. Xu, S. Chu, C. Cui, H. Ju, J. Zhu, Y. Lin, J. Shui and H. Liang, *Science*, 2021, **374**, 459–464.
42 Z. Wang, S. Chen, W. Wu, R. Chen, Y. Zhu, H. Jiang, L. Yu and N. Cheng, *Adv. Mater.*, 2023, **35**, 2301310.
43 W. Zeng, C. Wang, Q. Yan, P. Yin, L. Tong and H. Liang, *Nat. Commun.*, 2022, **13**, 7654.
44 T. Yoo, J. Yoo, A. Sinha, M. Bootharaju, E. Jung, H. Lee, B. Lee, J. Kim, W. Antink, Y. Kim, J. Lee, E. Lee, D. Lee, S. Cho, S. Yoo, Y. Sung and T. Hyeon, *J. Am. Chem. Soc.*, 2020, **142**, 14190–14200.
45 Y. Nakaya, F. Xing, H. Ham, K. Shimizu and S. Furukawa, *Angew. Chem., Int. Ed.*, 2021, **60**, 19715–19719.
46 W. He, X. Zhang, K. Zheng, C. Wu, Y. Pan, H. Li, L. Xu, R. Xu, W. Chen, Y. Liu, C. Wang, Z. Sun and S. Wei, *Angew. Chem., Int. Ed.*, 2023, **62**, e202213365.
47 Y. Zhang, Q. Zhao, B. Danil, W. Xiao and X. Yang, *Adv. Mater.*, 2024, **36**, 2400198.
48 X. Zheng, J. Yang, P. Li, Z. Jiang, P. Zhu, Q. Wang, J. Wu, E. Zhang, W. Sun, S. Dou, D. Wang and Y. Li, *Angew. Chem., Int. Ed.*, 2023, **62**, e202217449.
49 X. Zeng, Y. Jing, S. Gao, W. Zhang, Y. Zhang, H. Liu, C. Liang, C. Ji, Y. Rao, J. Wu, B. Wang, Y. Yao and S. Yang, *Nat. Commun.*, 2023, **14**, 7414.
50 H. Wang, X. Gu, X. Zheng, H. Pan, J. Zhu, S. Chen, L. Cao, W. X. Li and J. Lu, *Sci. Adv.*, 2019, **5**, eaat6413.
51 P. Yin, X. Luo, Y. Ma, S. Chu, S. Chen, X. Zheng, J. Lu, X. Wu and H. Liang, *Nat. Commun.*, 2021, **12**, 3135.
52 J. Wordsworth, T. M. Benedetti, S. V. Somerville, W. Schuhmann, R. D. Tilley and J. J. Gooding, *Angew. Chem., Int. Ed.*, 2022, **61**, e202200755.
53 X. Zhang, Z. Sun, R. Jin, C. Zhu, C. Zhao, Y. Lin, Q. Guan, L. Cao, H. Wang, S. Li, H. Yu, X. Liu, L. Wang, S. Wei, W. X. Li and J. Lu, *Nat. Commun.*, 2023, **14**, 530.
54 T. Song, C. Xu, Z. Sheng, H. Yan, L. Tong, J. Liu, W. Zeng, L. Zuo, P. Yin, M. Zuo, S. Chu, P. Chen and H. Liang, *Nat. Commun.*, 2022, **13**, 6521.
55 Y. Wang, Y. Yao, C. Xu, D. Tang, Y. Li, Z.-A. Qiao, H.-W. Liang and B. Liu, *Adv. Mater.*, 2024, 2416111.
56 A. Sfeir, C. A. Teles, C. Ciotonea, G. N. M. Reddy, M. Marinova, J. Dhainaut, A. Löfberg, J.-P. Dacquin, S. Royer and S. Laassiri, *Appl. Catal., B*, 2023, **325**, 122319.
57 V. Polshettiwar, *Acc. Chem. Res.*, 2022, **55**, 1395–1410.
58 S. Hu, J. Guan, R. Ma, Y. Tao, D. Liu, J. Gong and Y. Xiong, *Rare Met.*, 2024, **43**, 2331–2338.
59 H. Zheng, S. Wang, S. Liu, J. Wu, J. Guan, Q. Li, Y. Wang, Y. Tao, S. Hu, Y. Bai, J. Wang, X. Xiong, Y. Xiong and Y. Lei, *Adv. Funct. Mater.*, 2023, **33**, 2300815.
60 R. Ma, Q. Li, J. Yan, Y. Tao, S. Hu, D. Liu, J. Gong and Y. Xiong, *Nano Res.*, 2023, **16**, 9618–9624.
61 J. Guan, M. Wang, R. Ma, Q. Liu, X. Sun, Y. Xiong and X. Chen, *Sens. Actuators, B*, 2023, **375**, 132972.
62 Y. Xiong, H. Li, C. Liu, L. Zheng, C. Liu, J. O. Wang, S. Liu, Y. Han, L. Gu, J. Qian and D. Wang, *Adv. Mater.*, 2022, **34**, 2110653.
63 Y. Chai, S. Chen, Y. Chen, F. Wei, L. Cao, J. Lin, L. Li, X. Liu, S. Lin, X. Wang and T. Zhang, *J. Am. Chem. Soc.*, 2024, **146**, 263–273.
64 S. Kaneko and M. Kiguchi, *Fullerenes, Nanotubes Carbon Nanostruct.*, 2014, **22**, 166–172.
65 L. Deng, S. Liu, D. Liu, Y. M. Chang, L. Li, C. Li, Y. Sun, F. Hu, H. Y. Chen, H. Pan and S. Peng, *Small*, 2023, **19**, 2302238.
66 Z. Jiang, S. Ren, X. Cao, Q. Fan, R. Yu, J. Yang and J. Mao, *Angew. Chem., Int. Ed.*, 2024, **63**, e202408412.
67 Y. Hu, T. Chao, Y. Li, P. Liu, T. Zhao, G. Yu, C. Chen, X. Liang, H. L. Jin, S. Niu, W. Chen, D. Wang and Y. Li, *Angew. Chem., Int. Ed.*, 2023, **62**, e202308800.